CHEMISTRY

Methanol conversion on borocarbonitride catalysts: Identification and quantification of active sites

Xuefei Zhang[1], Pengqiang Yan[2], Junkang Xu[1], Fan Li[2], Felix Herold[3], Bastian J. M. Etzold[3], Peng Wang[1], Dang Sheng Su[2,4], Sen Lin[1]*, Wei Qi[2]*, Zailai Xie[1]*

Borocarbonitrides (BCNs) have emerged as highly selective catalysts for the oxidative dehydrogenation (ODH) reaction. However, there is a lack of in-depth understanding of the catalytic mechanism over BCN catalysts due to the complexity of the surface oxygen functional groups. Here, BCN nanotubes with multiple active sites are synthesized for oxygen-assisted methanol conversion reaction. The catalyst shows a notable activity improvement for methanol conversion (29%) with excellent selectivity to formaldehyde (54%). Kinetic measurements indicate that carboxylic acid groups on BCN are responsible for the formation of dimethyl ether, while the redox catalysis to formaldehyde occurs on both ketonic carbonyl and boron hydroxyl (B—OH) sites. The ODH reaction pathway on the B—OH site is further revealed by in situ infrared, x-ray absorption spectra, and density functional theory. The present work provides physical-chemical insights into the functional mechanism of BCN catalysts, paving the way for further development of the underexplored nonmetallic catalytic systems.

INTRODUCTION

With the depletion of fossil resources and the strict requirements of environmental protection and sustainable development, traditional chemical industry is facing severe upgrade to satisfy the growing population and energy demand. The idea of nonmetallic catalysis has attracted considerable attention over the past decade in the fields of chemistry and materials science (*1*), especially for nanocarbon materials, which have shown unique advantages, such as tunable surface acidity/basicity and electron density as well as earth abundance of carbon elements and reusability. Various types of nanocarbon materials (graphene, nanotubes, nanodiamond, etc.) have been applied in gas-phase (*2*) or liquid-phase (*3*) thermal catalysis and also electronic catalysis (*4*), such as oxidative dehydrogenation (ODH) of alkanes (*5*), selective oxidation of organics (*6*), and oxygen reduction reactions (*7*). However, the main challenge in enhancing stability and selectivity of carbon catalysts still exists, and developing previously unknown generations of nonmetallic catalysts is still the main research emphasis in related fields. For example, it has been reported very recently that boron nitride (BN) exhibits ultrahigh stability and alkene selectivity (>98%) in light alkane (propane or ethane, etc.) ODH reactions, which is considered as a new-generation "game-changing" catalytic material for selective ODH reactions (*8*). The promoted catalytic activity and stability of BN materials are generally believed to originate from their abundant edge sites in oxidation state and relatively high thermal conductivity (*9*–*12*). However, the well-defined reaction mechanism and the clear identification of active sites for BN catalysts are still beyond realization, which has hindered the further development and potential practical applications of BN catalytic materials.

One of the feasible methods to further promote the catalytic activity of BN is to introduce the carbon element leading to previously unknown borocarbonitride (BCN) materials (*13*). BCN hybrids tend to form isolated patches of hexagonal BN in graphene phases (at high B and N concentrations), the structure of which is thermodynamically favorable compared with homogeneous distribution of B, C, and N elements (*14*). The coexistence of graphene and BN domains in the same structure provides an ideal platform for identification, quantification, and comparison of the active sites; intrinsic activity; and detailed ODH reaction mechanism on carbon and BN materials. In addition, these BCN materials have extraordinary properties complementary to those of pure carbon and BN with a wide spectrum of changes in morphology, porosity, surface oxygen functional groups, and electronic structure (*15*). Introduction of graphene domain also facilitates the electron transportation process, and BCN materials could impart carbon catalysis to BN materials for several catalytic applications with notable activity enhancement (*16*, *17*). For example, BCN nanosheets exhibit both high activity and excellent oxidation resistance in ODH of ethylbenzene to styrene (*18*), as well as notable catalytic activity for oxygen reduction (*19*). However, the catalytic applications of BCN materials are still at an early proof of concept stage (*20*), and the molecular design and synthesis of BCN catalysts and quantification of the catalytic activity of each functionality remain to be explored (*21*).

Here, we developed a previously unknown and effective synthetic approach for BCN nanotubes (BCNNTs) via assembly and pyrolysis of small organic molecules. The nitrogen, boron, carbon, and oxygen content of the proposed BCNNT materials could be regulated in a wide range, which are considered as ideal platform catalysts to clarify the origin of the activity, similarity, and difference of nonmetallic carbon and BN materials. Oxygen-assisted methanol conversion to formaldehyde (FA) and dimethyl ether (DME) was performed on BCNNT catalysts to identify and quantify the origin of both acidic and redox catalytic activities. The proposed BCNNT catalysts exhibit a notable activity improvement for methanol conversion (29%) with enhanced FA selectivity (54%), superior to pure BNs or nanocarbons. The basic reaction kinetics of methanol conversion were systematically investigated, indicating the superiority of BCN compared with carbon and BN. The proposed active site identification and quantification strategy may also shed light on the establishment

[1]State Key Laboratory of Photocatalysis on Energy and Environment, College of Chemistry, Fuzhou University, Fuzhou 350016, China. [2]Shenyang National Laboratory for Materials Science, Institute of Metal Research, Chinese Academy of Sciences, Shenyang 110016, China. [3]Ernst-Berl-Institut für Technische und Makromolekulare Chemie, Technische Universität Darmstadt, 64287 Darmstadt, Germany. [4]Fritz-Haber-Institut der Max-Planck-Gesellschaft, Faradayweg 4-6, 14195 Berlin, Germany.
*Corresponding author. Email: zlxie@fzu.edu.cn (Z.X.); slin@fzu.edu.cn (S.L.); wqi@imr.ac.cn (W.Q.)

of structure-function relations, which would promote the development of novel BCN catalytic materials.

RESULTS AND DISCUSSION

Preparation and characterizations of catalysts

As shown in Fig. 1, BCNNTs were synthesized via a simple pyrolysis process using boric acid, urea, and polyethylene glycol (PEG) as boron, nitrogen, and carbon source and soft templates, respectively. The high-resolution transmission electron microscopy (HRTEM; Fig. 2, A and B) and scanning electron microscopy (SEM) images (fig. S1) suggest that the synthesized BCNNT catalysts are shaped as one-dimensional (1D) nanotubes with a mean external diameter of around 100 nm, and the thickness of the tube wall is 17 ± 3 nm. The selected-area electron diffraction (SAED) pattern mainly shows three reflections corresponding to (002), (100), and (110) planes of hexagonal graphitic structures with minor deviations due to defects and the incorporation of B and N elements. The diffused diffraction rings suggest the defective and polycrystalline nature of the nanotubes, in agreement with HRTEM observations (Fig. 2C). A *d* spacing of 0.35 nm could be observed in the graphitic region in HRTEM images, which is consistent with the value of $d = 0.348$ nm from the powder x-ray diffraction (XRD) data (fig. S2), corresponding to the (002) plane of typical turbostratic graphitic carbons. The elemental mapping analysis of the synthesized BCN tubes reveals the presence of the elements B, N, C, and O (Fig. 2, D to G). The Brunauer-Emmett-Teller (BET) surface area and pore size distribution of the synthesized BCN tubes are 914 $m^2 g^{-1}$ and 0.5 to 3 nm, respectively, based on nitrogen adsorption isotherms (fig. S3). The boron, nitrogen, and carbon content could be adjusted from 25 to 40%, 20 to 60%, and 10 to 50%, respectively, by regulating the dosage of the precursors. The relatively simple synthesis procedure and low cost shed light on the potential industrial applications of BCNNT catalysts.

The attenuated total reflection–infrared (IR) spectra of the BCNNT samples (fig. S4) exhibit broad bands at 1387 cm^{-1} (B—N in-plane transverse stretching), 1244 cm^{-1} (C—N stretching), 789 cm^{-1} (B—N bending) (*22*–*24*), 3670 cm^{-1} (O—H stretching), 1060 cm^{-1} (B—C stretching) (*25*), and 890 cm^{-1} (B—O out-plane bending) (*26*), indicating the formation of a ternary hybrid system of BCNNTs. The surface oxygen content and concentration of different oxygen functional groups can be adjusted (as shown in table S1 and fig. S5) through calcination of the BCNNTs in air under different temperatures (from 280° to 380°C) for a given time, and the obtained catalysts were denoted as BCNNTs-*X*, where *X* represents the calcination temperature.

Catalytic performance

Methanol conversion in the presence of oxygen, which is considered as an important type of reactions in chemical industry, was performed on the synthesized BCNNT samples to evaluate their acidic and redox catalytic properties. The reaction was run under relatively gentle conditions (573 K) to ensure the structural integrity of BCNNT catalysts (fig. S6). First, the content of B, C, and N was optimized on the basis of the comparisons of the catalytic activity for different BCN samples with various B/C/N ratios (table S2), which were synthesized by changing the dosage of precursors. The BCNNTs with a PEG dosage of 1.0 g were selected as the catalysts for the following kinetic analysis, because they have the highest activity (fig. S7). As shown in Fig. 3A, the main products of the reaction on BCNNTs are FA (~47%) from ODH, DME (~14%) from intermolecular dehydration, CO_2 (~35%) from deep oxidation (combustion), and slight dimethoxymethane (DMM; ~3%) from secondary reaction. Methanol conversion could reach ~25% with the carbon balance at 100 ± 5% under the chosen reaction conditions, and BCNNT catalysts are stable for at least 20 hours, which was confirmed by IR, XRD, SEM, and TEM characterizations on the used catalysts (figs. S8 and S9). The x-ray photoelectron spectroscopy (XPS) measurements on the fresh and spent BCNNT catalysts (as shown in tables S3 and S4 and fig. S10) demonstrate that there is no significant change in the identity and quantity of oxygen functionalities during the reaction, indicating the relatively high structural stability of the catalysts. As shown in Fig. 3B, methanol conversion reactions were also performed on BN and oxidized carbon nanotube (OCNT) catalysts under the same reaction conditions for comparisons (fig. S11). The main products of methanol conversion on BN are FA (80%), CO_2 (20%), and negligible DME at a very low conversion (2%), while both ODH and dehydration reactions could be observed on OCNT catalysts because of the existence of acid and redox sites. Methanol conversion on OCNT could reach 9%, with the selectivity of FA, DME, DMM, and CO_2 at 49, 23, 4, and 24%, respectively. The higher

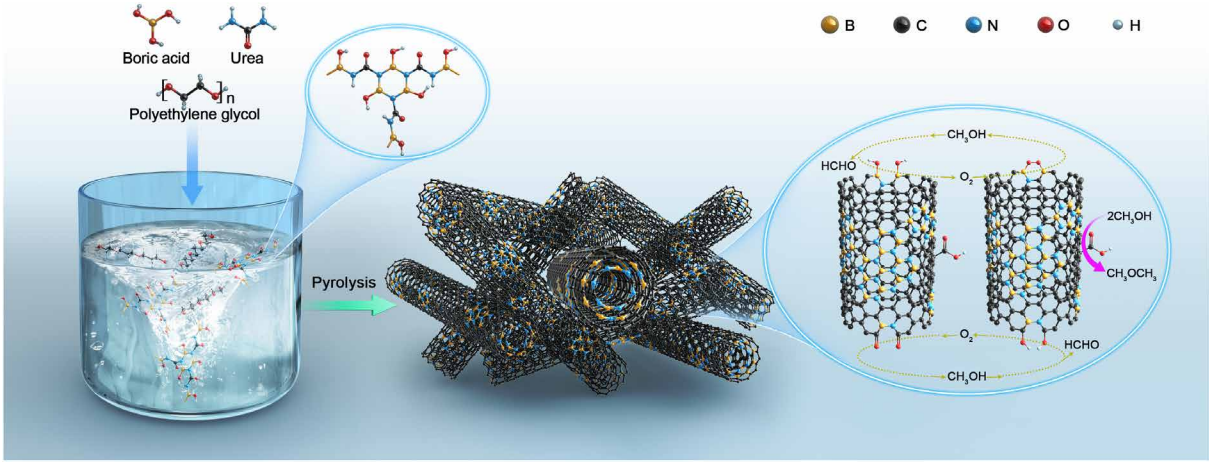

Fig. 1. Schematic illustration of the preparation procedure of BCNNTs (left) and the proposed reaction pathways (right) for methanol conversion.

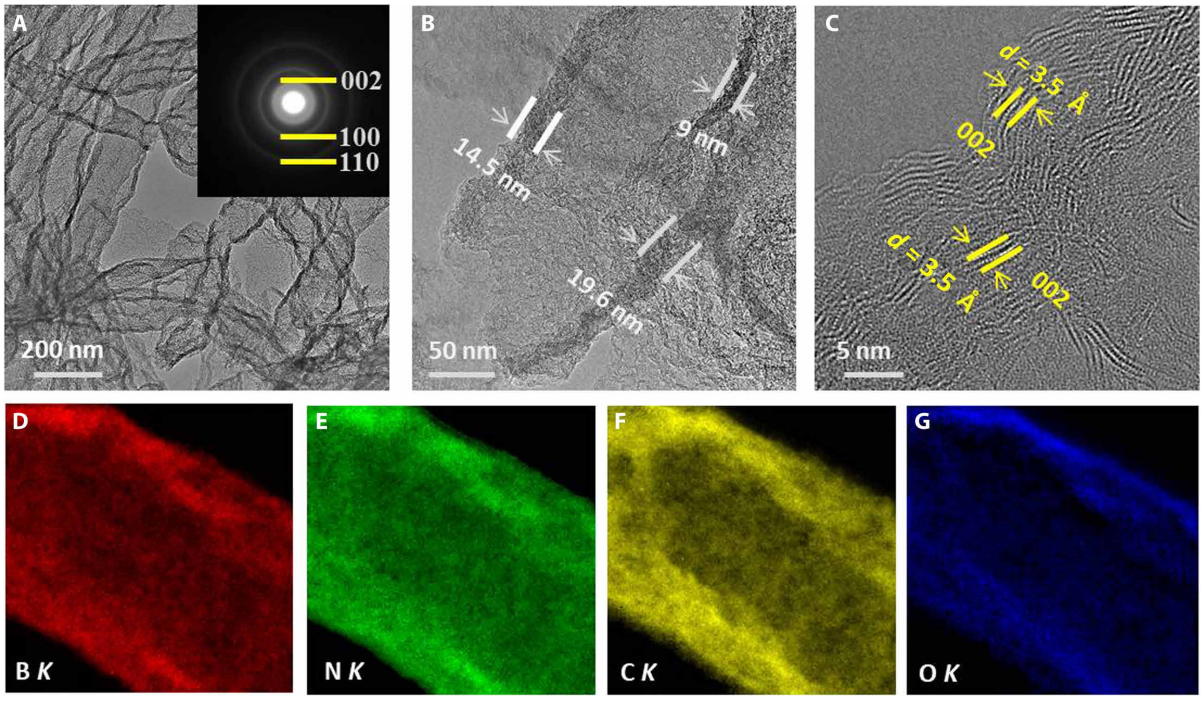

Fig. 2. Structure characterization of BCNNTs. (**A** to **C**) TEM and HRTEM images and (**D** to **G**) energy-filtered TEM elemental mapping images of BCNNTs.

catalytic activity and target product selectivity of BCNNT catalysts compared with BN and OCNT materials suggest the synergy effect of BN and graphitic carbon components in the hybrids. The advantage of the synergy of carbon and BN species was also revealed by the electron paramagnetic resonance (EPR) measurements. The strong EPR signals for both fresh and spent BCNNT catalysts (fig. S12) suggest the generation of unpaired electrons, which may facilitate methanol ODH reactions.

As shown in Table 1, BCNNT catalysts exhibit superior or at least comparable catalytic activity compared with the most typical metal catalysts, but they are still not as good as the industrial Ag catalyst and MoFe catalysts (*27*–*34*). Considering the gentle reaction condition and sustainable nature, BCNNT materials exhibit great potential in substituting conventional metal-based catalysts in ODH reactions of methanol producing FA.

The apparent activation energy for methanol ODH on BCNNTs is 81 kJ mol^{-1} from Arrhenius equation, which is slightly lower than that on conventional metal-based catalysts (for example, TiO_2 nanocrystals at 88 kJ mol^{-1}) (*28*). The reaction order of O_2 is 0.41 for BCNNT-catalyzed methanol ODH reactions (fig. S13), which is similar to that of BCN nanosheets in ethylbenzene ODH reactions (0.17 to 0.57) (*18*). As shown in Fig. 3C, the selectivity of the target products FA and DME changes with surface oxygen content of BCNNTs, suggesting that the reactivity (both acid and redox) may originate from surface oxygen functionalities. Meanwhile, we found that the selectivity of FA, DME, and CO_2 had negligible change with different conversions under constant reaction temperature (fig. S14), indicating that methanol conversion on BCNNTs is a parallel reaction.

Identification and quantification of active sites

The catalytic activity was linked to the chemical structure to reveal the active sites on BCNNTs for dehydration and ODH reactions (Fig. 4A). The surface concentration of different oxygen functional groups (—COOH, —C═O, —B—OH, and —C—OH) on BCNNT catalysts was determined by O1s XPS analysis (as shown in table S1). A positive linear dependence of DME formation rates on the surface concentration of carboxylic acid (—COOH) groups could be observed in Fig. 4B, suggesting that intermolecular dehydration of methanol (forming DME) may occur only on these acid sites exhibiting the highest acidity among surface oxygen functionalities on BCNNTs. The intrinsic catalytic activity of carboxylic acid (—COOH) groups for DME formation [turnover frequency (TOF)] is 4.59×10^{-6} molecules $COOH^{-1}$ s^{-1} from the slope of the line in Fig. 4B. In contrast, FA formation rates have shown no such linear dependence on a single type of oxygen functionality (fig. S15), indicating the methanol ODH reactions may relate to multiple active sites. We assumed that the methanol ODH reactions on each type of active sites do not influence other groups (non-competitive or non-synergistic reactions) and the intrinsic activity could be different for various sites. The experimentally observed FA formation rates were linearly fitted with the surface concentration of different oxygen functional groups (—C═O, —C—OH, —COOH, and —B—OH) using TOF as fitting parameters. After testing all the possible combinations of different oxygen functionalities, the best fitting could be achieved when ketonic carbonyl (C═O) and boron hydroxyl (B—OH) groups were both simultaneously considered as active sites (the detailed fitting process can be found in note S1). As shown in Fig. 4C, the simulated FA formation rate (r'_{FA}) fits well with the experimentally observed rate value (r_{FA}), and the TOF methanol ODH reactions on —C═O and —B—OH could be calculated via the slope of the line, as shown in Fig. 4D. It is reasonable that —C═O (ketonic carbonyl) groups on carbon could catalyze methanol ODH reactions, because they are also found to be the active sites for the alkane ODH process (*35*, *36*). The nucleophilic ketonic carbonyl groups would abstract two hydrogen atoms from methyl and hydroxyl groups of methanol molecules, respectively. The reduced

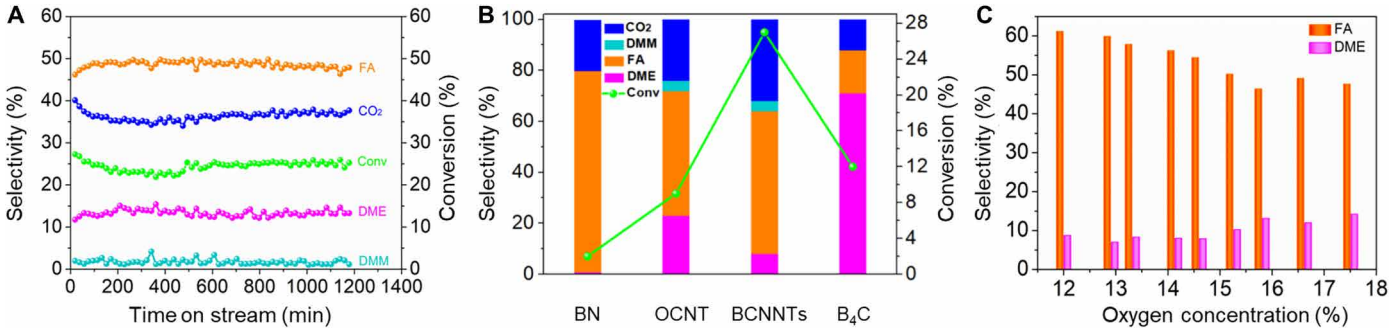

Fig. 3. Catalytic activity measurements and comparisons. (**A**) Methanol conversion activity of BCNNTs-360°C as a function of reaction time. (**B**) Methanol conversion activity of BN, OCNT, BCNNTs-320°C, and B_4C catalysts (reaction conditions: 1 kPa of methanol; 8 kPa of O_2, 573 K, 100 mg of catalysts, balance He). (**C**) Steady-state catalytic activities (573 K) of BCNNT catalysts with different oxygen contents (calcination temperature).

Table 1. Catalytic activity comparison. Catalytic activity of BCNNTs compared with that of metal-based catalysts.

No.	Catalysts	*T* (K)	Mass (g)	P_{O2}/P_{CH3OH}	Conversion (%)	Selectivity (FA, %)	Reference
1	BCNNTs	573	0.10	8:1	29	54	This work
2	Au-NbMCF	573	0.12	8:4	20	61	27
3	TiO_2-300C	573	0.025	5:1	28	7	28
4	V-Mg-O	573	–	1:1	30	99	29
5	$MoOx/SiO_2$	476	3.1	47:6	20	89	30
6	V_2O_5/TiO_2	433	0.20	16:5	41	61	31
7	Cu/SBA-3	523	0.02	2:1	8	47	32
8	$MoOx\text{-}Fe_2O_3$	498	–	10:1	90	92	33
9	ZrMCF	573	0.12	8:4	6	15	27
10	Ag/SiO_2	913	2.0	0.51:1	96	89	34

catalysts (with hydroxyl groups on the surface) would be reoxidized with the assistance of oxygen molecules forming FA and H_2O as products similar to the alkane ODH reaction process (*1*).

Mechanism of methanol ODH reactions on B—OH sites

The kinetic analysis above reveals that B—OH sites are also active for methanol ODH reactions, which is a new finding in nonmetallic catalysis. As shown in Fig. 5 (A and B), in situ diffuse reflectance infrared flourier transform spectra (DRIFTS) analysis (fig. S16) was performed on the "working" surface of BCNNT materials to clarify this catalytic process. Unlike —C═O groups, there is an obvious increase on the IR signal of —B—O at 930 cm^{-1} (—B—O out-plane mode shown in Fig. 5A) upon the solely introduction of O_2 into the reaction system, because the edge boron and B—OH sites are converted to B—O—O—B species and H_2O with the assistance of oxygen (*37*, *38*). The IR signal of B—O groups exhibits a remarkable decrease after switching the reactant inlet from O_2 to methanol, because B—O—O—B species could be reduced to B—OH sites to finish the redox cycle, and this transformation (redox cycle) is reversible as shown in Fig. 5B.

X-ray absorption spectroscopy (XAS) measurements were performed to further reveal the catalytic reaction process. As shown in Fig. 5C, there are six peaks in the B K-edge XAS spectra of BCNNT samples located at 189.8 eV (B1), 191.2 eV (B2), 191.8 eV (B3), 192.4 eV (B4), 193.3 eV (B5), and 198.8 eV (B6). These peaks can be assigned as B4C, BN3, BN2, BN, and B—O configuration π* state and B═N configuration σ* state (*39*), respectively. Reaction of oxygen with BCNNT samples (573 K) leads to a significant increase of the B—O signal, suggesting that B edge sites may be activated (oxidized) by oxygen molecules, which agrees well with in situ DRIFTS observations. On the contrary, there is neither N—O nor any other signal evolution (N═C π* state at 397.3 eV, N═B π* state at 399.3 eV, N═B σ* state at 405.6 eV, and N═C σ* state at 413.6 eV) (*40*–*42*) after reaction with oxygen and methanol (Fig. 5D), indicating that nitrogen species may not directly serve as active sites for the catalytic reaction. Combining the kinetic analysis and the spectroscopic data, we can draw a clear picture on the mechanism of methanol ODH reactions on B—OH sites. The B—OH sites may first be oxidized by molecular oxygen forming B—O—O—B species. The two hydrogen atoms from C—H and O—H bonds of methanol molecules are abstracted by B—O—O—B intermediates, forming FA as products. Meanwhile, the catalyst recovers to its original state (B—OH site) to finish the reaction cycle. The intrinsic methanol ODH catalytic activity (TOF) of B—OH is slightly higher than that of C═O (1.74×10^{-5} molecules B-OH^{-1} s^{-1} versus 1.45×10^{-5} molecules C═O^{-1} s^{-1}) under the same reaction conditions. The general reaction pathways for BCN-catalyzed methanol conversion are summarized in Fig. 1 (reaction pathways).

To achieve comprehensive understandings on the origin of the catalytic behavior of such a previously unknown and unique catalyst system, density functional theory (DFT) was carried out. Our calculation results indicate that the B—O—O—B formation step on BN without

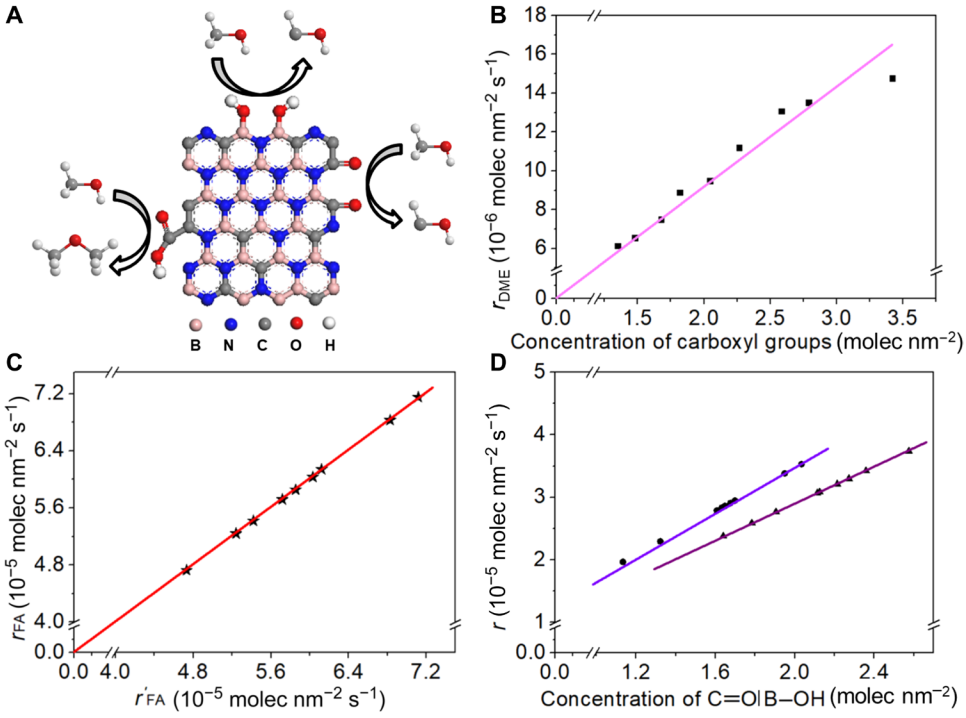

Fig. 4. Identification and quantification of active sites over BCNNT-catalyzed methanol conversion reaction. (**A**) Schematic illustration for methanol ODH and dehydration reaction on active sites. (**B**) DME formation rate (■) as a function of the surface concentration of —COOH. (**C**) Correlation between experimental (r_{FA}) and simulated (r'_{FA} = TOF(C=O)·[C=O] + TOF(B—OH)·[B—OH]) FA formation rate (★). (**D**) Simulated FA formation rate as a function of the surface concentration of —C=O (●) and —B—OH (▲). Reaction conditions: 1 kPa of methanol, 8 kPa of O_2, 573 K, 100 mg of catalysts, balance He.

carbon doping (Fig. 6A; C_0) has an extremely positive free energy change (ΔG) of 1.77 eV (Fig. 6B). Clearly, it is the rate-determining step in the overall pathway (fig. S17) due to the strong O—H bond, and the free energies of methanol ODH intermediates are shown in fig. S18. Therefore, the catalytic activity of each specified BCN configuration can be preliminarily assessed using the free energy change ($\Delta G_{B\text{-}O\text{-}O\text{-}B}$) for the dehydrogenation step of 2 (B—OH) to B—O—O—B. A more negative $\Delta G_{B\text{-}O\text{-}O\text{-}B}$ indicates that it is easier to dehydrogenate to form B—O—O—B intermediate.

Given that carbon doping could improve the catalytic performance of BN by tuning the electronic structures of active sites, we investigate the influence of carbon doping by replacing N or B atoms near the region of B—O—O—B active site on the activity of methanol ODH reactions. Our calculation results indicate that when a C atom is doped by replacing an adjacent N atom (N_a) of B—O—O—B (Fig. 6A; C_1), $\Delta G_{B\text{-}O\text{-}O\text{-}B}$ can be notable reduced to 1.21 eV compared to that (1.77 eV) for C_0 (Fig. 6B). When two C atoms are doped by replacing two N_a (Fig. 6A; C_2) of B—O—O—B, $\Delta G_{B\text{-}O\text{-}O\text{-}B}$ can be further lowered to 0.5 eV (Fig. 6B). In this case, after the formation of B—O—O—B, the adsorption of CH_3OH generates a ΔG of 0.47 eV (Fig. 6C). Subsequently, the dehydrogenation of CH_3OH to produce CH_2O species yields a very negative ΔG of −3.16 eV, recovering the catalyst with B—OH sites. When a C atom is doped by replacing an N atom (N_m) in the middle of B—O—O—B (Fig. 6A; C_1*), $\Delta G_{B\text{-}O\text{-}O\text{-}B}$ (1.69 eV; Fig. 6B) is nearly unchanged, compared to that for C_0. Similar results can be found for the case of two C atoms doping with the N_m substituted by one C atom (Fig. 6A; C_2*), for which the calculated $\Delta G_{B\text{-}O\text{-}O\text{-}B}$ is as high as 1.65 eV. The results are in agreement with experimentally observed boron carbide (B_4C) catalytic property (Fig. 3B) at ~12% methanol conversion with FA (17%), DME (71%), and CO_2 (12%). We also noticed that, when the number of doped carbon atoms is increased to 8, 15, and 20 (fig. S19; C_8, C_{15}, and C_{20}) without replacing N atoms, $\Delta G_{B\text{-}O\text{-}O\text{-}B}$ is even higher than 2 eV (fig. S20). Therefore, it is concluded that carbon doping can help to reduce $\Delta G_{B\text{-}O\text{-}O\text{-}B}$ with the increasing amount of carbon, assuming that the carbon atoms are doped into the appropriate lattice positions.

Density of states (DOS) analysis was performed to gain more physical insights for the carbon-doped B—OH sites. The hybridization between the electronic states of B—OH and between the electronic states of OH and B atom would trigger the splitting of hybridized energy levels into antibonding states and bonding states. In this case, the higher location of *p*-band center (see Materials and Methods for details) of B atom would correspondingly lead to a higher location of antibonding states with a lower occupancy, resulting in a stronger interaction between B and O. This means that the interaction between O and H would be weakened because of the decrease of the electron density on O. Therefore, the position of *p*-band center is a good descriptor of the binding strength of H on O: A higher location of *p*-band center facilitates the dehydrogenation of B—OH. Figure 6D shows the projected DOS for the *p* orbitals of the active B of the three carbon-doped BN (C_0, C_1, and C_2). The *p*-band center (−5.83 eV) of C_0 is far from the Fermi level (0 eV). Therefore, the O—H bond should be very strong, which leads to a highly positive $\Delta G_{B\text{-}O\text{-}O\text{-}B}$ of 1.77 eV. For C_1, the *p*-band center is significantly raised to −5.35 eV. In this case, the interaction between O and H becomes weaker, thus resulting in a less positive $\Delta G_{B\text{-}O\text{-}O\text{-}B}$ of 1.21 eV. For C_2, the *p*-band center is sharply lifted up to −3.92 eV, which leads to an

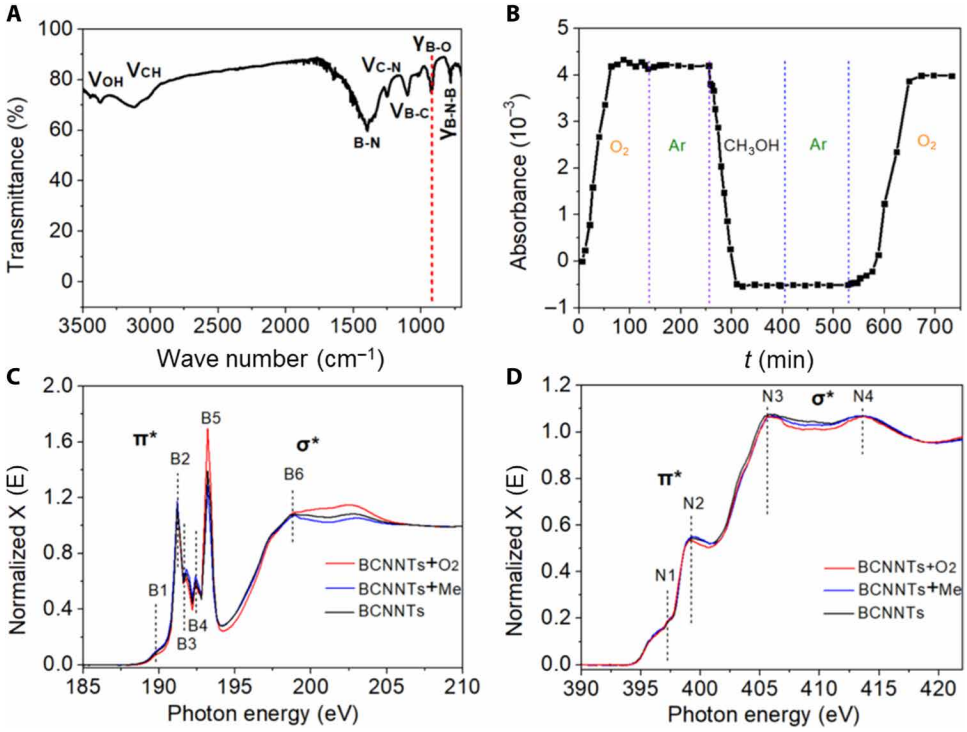

Fig. 5. Mechanism of methanol ODH reactions on B—OH site. (**A**) DRIFTS of BCNNTs-340°C. (**B**) IR signal intensity at 930 cm^{-1} (—B—O) of BCNNTs-340°C upon the introduction of O_2 and methanol during in situ DRIFT measurements. (**C**) B K-edge and (**D**) N K-edge XAS of fresh BCNNTs and the samples after reaction with O_2 and methanol, respectively.

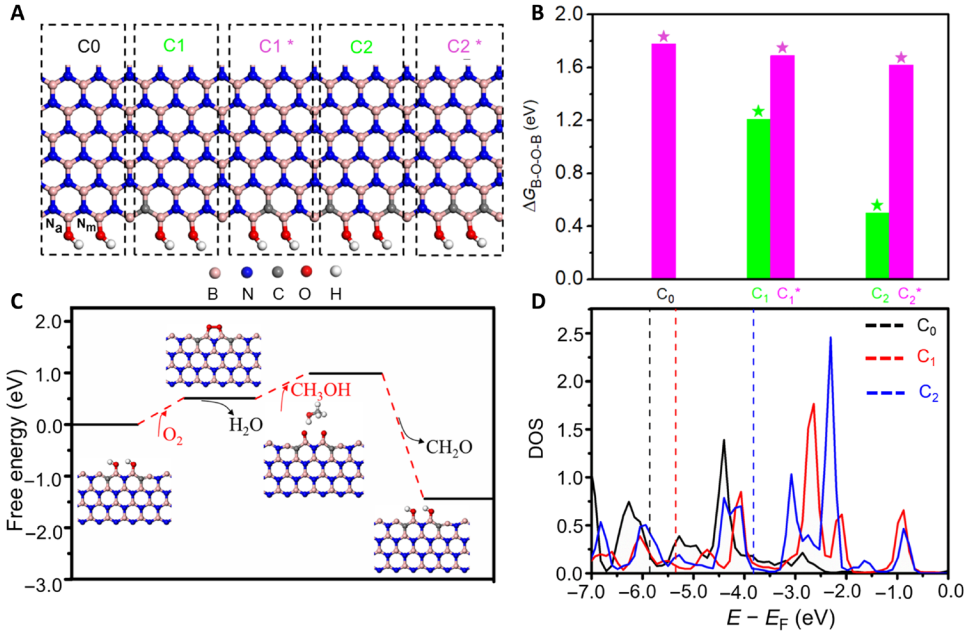

Fig. 6. DFT analysis for BCNNT catalysis. (**A**) Schematic of the computational models of C_0, C_1, C_1*, C_2, and C_2*. Gray (black), pink, red, blue, and white balls represent C, B, O, N, and H atoms, respectively. (**B**) Calculated $\Delta G_{B\text{-}O\text{-}O\text{-}B}$ for the rate-determining step on C_0, C_1, C_1*, C_2, and C_2*. (**C**) Calculated free-energy diagram for ODH reduction over C_2 system. The insets are the optimized structures of the intermediates along the reaction path. (**D**) Calculated projected DOS for 2*p* orbitals of the B of C_0, C_1, and C_2 systems. All energy levels are relative to the Fermi level for each system, which is set to zero. The energy levels with the *p*-band center of C_0, C_1, and C_2 are highlighted in black, red, and blue dashed lines, respectively.

optimal $\Delta G_{B\text{-}O\text{-}O\text{-}B}$ of 0.5 eV. Such a value suggests that the B—O—O—B intermediate can be easily formed on C_2. To this end, our theoretical results are in good agreement with the experimental observations and provide a useful strategy for synthesizing efficient BCN catalysts for methanol ODH reactions: The carbon atoms should be doped into the N lattice adjacent to B—O—O—B sites of the BN substrate, while the formation of B—C—B pair by substituting N_m with C should be suppressed.

CONCLUSION

In summary, we presented here a facile synthetic strategy to prepare BCNNTs from small-molecule organic precursors at low cost, which exhibit superior catalytic activity and stability in methanol conversion reactions relative to nonmetallic carbon, BN, and/or metal-based catalysts. The proposed BCNNTs exhibit high surface area, controllable chemical compositions, and adjustable oxygen functional groups (C═O, COOH, B—OH, and OH), which benefit the heterogeneous catalytic reaction process. We revealed here the origin of the catalytic activity of BCN materials with kinetic and spectroscopic evidences, as well as DFT calculation results. The acid catalysis (intermolecular dehydration of methanol to DME) happens on carboxylic acid groups, while the redox catalysis (ODH of methanol to FA) occurs on both ketonic carbonyl and boron hydroxyl sites. Moreover, the reaction pathways of methanol ODH on C═O and B—OH sites are different, but the intrinsic activity on these sites is similar. We believe that these research results could provide new physical-chemical insights into the reaction mechanism of nonmetallic catalytic systems and shed light on the detailed quantitative understandings on the nonmetallic BCN catalytic process.

MATERIALS AND METHODS

Materials preparation

Synthesis of BCNNTs with different B, C, and N content

Boric acid (0.3 g), urea (10.0 g), and PEG (0.3, 0.6, 1.0, and 1.2 g) (molecular weight, 2000) were dissolved in 80 ml of deionized water. The homogeneous solution was heated to 120°C for 10 hours under stirring before recrystallization. A white crystalline powder was obtained upon evaporation of the solvent. The obtained solid mixture was annealed at 900°C for 6 hours with a heating rate of 5°C/min under the protection of nitrogen, and the obtained final products were named as BCN-0.3, BCN-0.6, BCN-1.0 (BCNNTs), and BCN-1.2.

Synthesis of BCNNTs with different oxygen contents

BCNNTs (150 mg) were calcined at a given temperature for a certain time in air, yielding BCNNT samples with different oxygen contents. The synthesized samples are named BCNNTs-*X*-*Y*, where *X* represents the calcination temperature (*X* = 280°, 300°, 310°, 320°, 330°, 340°, 350°, 360°, and 380°C) and *Y* is the calcination time (1, 2, 2.5, 3, 3.5, 4, 4.5, 5, and 6 hours).

Synthesis of h-BN

Boric acid (0.927 g) and urea (27 g) were dissolved in 100 ml of deionized water. The homogeneous solution was heated to 120°C for 10 hours under stirring to recrystallization. The white crystalline powder formed with the evaporation of solvents. The precursor was heated to 900°C with a ramping rate of 5°C/min and kept for 2 hours under N_2 protection, and the obtained final products were denoted as BN.

Synthesis of OCNT

Primary CNT (0.2 g) and concentrated nitric acid (200 ml) were mixed in a 500-ml round-bottom flask. The mixture was heated to 120°C to reflux for 2 hours, and the precipitate was filtered out and washed with deionized water for several times until the pH of the filtrate reached 7. The product was dried in vacuum at 120°C for 24 hours to give black OCNTs.

Catalyst characterizations

Powder XRD patterns were collected on a Bruker D8 ADVANCE diffractometer with Cu-K1 radiation (λ = 1.5406 Å). Data were obtained with a scanning speed of 15°/min in the range of 10° to 80°. TEM measurements were performed on an aberration-corrected JEOL ARM 200CF microscope, and SAED and EDX (energy-dispersive x-ray) elemental mapping measurements were performed on the same TEM. The XPS spectra were obtained from a surface analysis system (ESCALAB 250, Thermo VG, USA) with Al-Ka x-rays (1486.6 eV, 150 W, 50.0 eV pass energy). The O1s bands were deconvoluted into four bands at binding energies of 531.2 to 531.3, 532.3 to 532.4, 532.7 to 532.8, and 533.6 to 533.7 eV using CasaXPS software with a full width at half maximum of 1.2 to 1.5 eV, corresponding to C═O, COOH, B—O(H), and C—OH groups, respectively. N_2 adsorption-desorption isotherms were measured at −196°C using Micromeritics ASAP 2020 instrument, and the pore size distribution was calculated by DFT. The DRIFTS were recorded on a Thermo Fisher Scientific Nicolet iS 10 Fourier transform IR spectrometer (temperature, 300°C; 10 ml/min 0.5% O_2; 10 ml/min 13% methanol; balance Ar). The thermogravimetric analysis was performed on NETZSCH STA 449 C with temperature in the range of 40° to 800°C in air. The EPR was carried out on Bruker A300 at 20°C. The x-ray adsorption fine structure spectra (B and N K-edge) were collected at the Hefei National Synchrotron Radiation Laboratory.

DFT calculation details

All calculations were performed using the Vienna Ab Initio Simulation Package (VASP) based on plane-wave basis sets (*43*). Projector-augmented wave potentials were used for modeling electron-ion interactions, with a plane-wave energy cutoff set to 500 eV. The generalized gradient approximation with the Perdew-Burke-Ernzerhof (PBE) functional was adopted for structural optimization (*44*). The surface Brillouin zone is sampled with a 1 × 3 × 1 uniform mesh for the surface optimization, while it is set to be 9 × 9 × 1 for the electronic structure calculations (*45*). All the surfaces are fully relaxed by using a nonlinear conjugate gradient algorithm until total energy and atomic forces are converged within error tolerances of 10^{-5} eV and 0.01 eV/Å, respectively. Free energy calculations of ODH on BN-based surfaces followed a standard hydrogen electrode model suggested by Nørskov *et al.* (*46*). The free energy change (Δ*G*) is defined (*47*)

$$\Delta G = \Delta E + \Delta ZPE - T\Delta S + \Delta G_U$$

where Δ*E* is the electronic energy change directly, Δ*ZPE* is the zero-point energy change, *T* is the temperature (298 K), and Δ*S* is the entropy change. The vibrational frequencies are calculated to determine ZPE and the entropy contributions.

Methanol conversion reaction and catalytic activity measurement

Methanol ODH and intermolecular dehydration conversion rates were measured on 100 mg of BCNNT or other catalysts at atmospheric pressure at 573 K using a tubular quartz flow reactor with plug flow. Reactant mixtures contained methanol (99.9%), O_2 (99.999%), and He (99.999%) at a typical gas flow rate of 6000 ml hour^{-1} of gas per gram of catalyst used, and the molar flow rates of them were adjusted to give the desired methanol and O_2 partial pressures (0.05 to 0.8 kPa and 0.05 to 1.6 kPa, respectively). Reactant and product concentrations were analyzed on-line with a gas chromatograph (SP-2100A, Beijing Ruili) equipped with a thermal conductivity detector and a flame ionization detector.

SUPPLEMENTARY MATERIALS

Supplementary material for this article is available at http://advances.sciencemag.org/cgi/content/full/6/26/eaba5778/DC1

REFERENCES AND NOTES

1. W. Qi, P. Yan, D. S. Su, Oxidative dehydrogenation on nanocarbon: Insights into the reaction mechanism and kinetics via in situ experimental methods. *Acc. Chem. Res.* **51**, 640–648 (2018).
2. J. Zhang, D. Su, A. Zhang, D. Wang, R. Schlögl, C. Hébert, Nanocarbon as robust catalyst: Mechanistic insight into carbon-mediated catalysis. *Angew. Chem. Int. Ed.* **119**, 7460–7464 (2007).
3. W. Qi, W. Liu, S. Liu, B. Zhang, X. Gu, X. Guo, D. Su, Heteropoly acid/carbon nanotube hybrid materials as efficient solid-acid catalysts. *ChemCatChem* **6**, 2613–2620 (2014).
4. Y. Zheng, Y. Jiao, Y. Zhu, L. H. Li, Y. Han, Y. Chen, A. Du, M. Jaroniec, S. Z. Qiao, Hydrogen evolution by a metal-free electrocatalyst. *Nat. Commun.* **5**, 3783 (2014).
5. W. Qi, D. Su, Metal-free carbon catalysts for oxidative dehydrogenation reactions. *ACS Catal.* **4**, 3212–3218 (2014).
6. G. Wen, S. Wu, B. Li, C. Dai, D. S. Su, Active sites and mechanisms for direct oxidation of benzene to phenol over carbon catalysts. *Angew. Chem. Int. Ed.* **54**, 4105–4109 (2015).
7. K. Mamtani, D. Jain, D. Dogu, V. Gustin, S. Gunduz, A. C. Co, U. S. Ozkan, Insights into oxygen reduction reaction (ORR) and oxygen evolution reaction (OER) active sites for nitrogen-doped carbon nanostructures (CN_x) in acidic media. *Appl. Catal. Environ.* **220**, 88–97 (2018).
8. J. T. Grant, C. A. Carrero, F. Goeltl, J. Venegas, P. Mueller, S. P. Burt, S. E. Specht, W. P. McDermott, A. Chieregato, I. Hermans, Selective oxidative dehydrogenation of propane to propene using boron nitride catalysts. *Science* **354**, 1570–1573 (2016).
9. L. Shi, D. Wang, W. Song, D. Shao, W.-P. Zhang, A.-H. Lu, Edge-hydroxylated boron nitride for oxidative dehydrogenation of propane to propylene. *ChemCatChem* **9**, 1788–1793 (2017).
10. A. M. Love, B. Thomas, S. E. Specht, M. P. Hanrahan, J. M. Venegas, S. P. Burt, J. T. Grant, M. C. Cendejas, W. P. McDermott, A. J. Rossini, I. Hermans, Probing the transformation of boron nitride catalysts under oxidative dehydrogenation conditions. *J. Am. Chem. Soc.* **141**, 182–190 (2019).
11. J. T. Grant, W. P. McDermott, J. M. Venegas, S. P. Burt, J. Micka, S. P. Phivilay, C. A. Carrero, I. Hermans, Boron and boron-containing catalysts for the oxidative dehydrogenation of propane. *ChemCatChem* **9**, 3623–3626 (2017).
12. J. M. Venegas, W. P. McDermott, I. Hermans, Serendipity in catalysis Research: Boron-based materials for alkane oxidative dehydrogenation. *Acc. Chem. Res.* **51**, 2556–2564 (2018).
13. X. Li, B. Lin, H. Li, Q. Yu, Y. Ge, X. Jin, X. Liu, Y. Zhou, J. Xiao, Carbon doped hexagonal BN as a highly efficient metal-free base catalyst for Knoevenagel condensation reaction. *Appl. Catal. Environ.* **239**, 254–259 (2018).
14. S. Chen, Z. Chen, S. Siahrostami, D. Higgins, D. Nordlund, D. Sokaras, T. R. Kim, Y. Liu, X. Yan, E. Nilsson, R. Sinclair, J. K. Nørskov, T. F. Jaramillo, Z. Bao, Designing boron nitride islands in carbon materials for efficient electrochemical synthesis of hydrogen peroxide. *J. Am. Chem. Soc.* **140**, 7851–7859 (2018).
15. L. S. Panchakarla, K. S. Subrahmanyam, S. K. Saha, A. Govindaraj, H. R. Krishnamurthy, U. V. Waghmare, C. N. R. Rao, Synthesis, Structure, and Properties of Boron- and Nitrogen-Doped Graphene. *Adv. Mater.* **21**, 4726–4730 (2009).
16. M. Zheng, J. Shi, T. Yuan, X. Wang, Metal-free dehydrogenation of N-heterocycles by ternary *h*-BCN nanosheets with visible light. *Angew. Chem. Int. Ed. Engl.* **57**, 5487–5491 (2018).
17. J. Jin, F. Pan, L. Jiang, X. Fu, A. Liang, Z. Wei, J. Zhang, G. Sun, Catalyst-free synthesis of crumpled boron and nitrogen co-doped graphite layers with tunable bond structure for oxygen reduction reaction. *ACS Nano* **8**, 3313–3321 (2014).
18. F. Guo, P. Yang, Z. Pan, X.-N. Cao, Z. Xie, X. Wang, Carbon-doped BN nanosheets for the oxidative dehydrogenation of ethylbenzene. *Angew. Chem. Int. Ed. Engl.* **56**, 8231–8235 (2017).
19. H. Tabassum, R. Zhou, A. Mahmood, Z. Liang, S. Guo, A catalyst-free synthesis of B, N co-doped graphene nanostructures with tunable dimensions as highly efficient metal free dual electrocatalysts. *J. Mater. Chem. A* **4**, 16469–16475 (2016).
20. Y. Zhao, L. Yang, S. Chen, X. Wang, Y. Ma, Q. Wu, Y. Jiang, W. Qian, Z. Hu, Can boron and nitrogen co-doping improve oxygen reduction reaction activity of carbon nanotubes? *J. Am. Chem. Soc.* **135**, 1201–1204 (2013).
21. H. Tabassum, W. Guo, W. Meng, A. Mahmood, R. Zhao, Q. Wang, R. Zou, Metal–organic frameworks derived cobalt phosphide architecture encapsulated into B/N Co-doped graphene nanotubes for all pH value electrochemical hydrogen evolution. *Adv. Energy Mater.* **7**, 160671 (2017).
22. M. Li, W. Zhu, P. Zhang, Y. Chao, Q. He, B. Yang, H. Li, A. Borisevich, S. Dai, Graphene-analogues boron nitride nanosheets confining ionic liquids: A high-performance quasi-liquid solid electrolyte. *Small* **12**, 3535–3542 (2016).
23. C. Lv, Y. Qian, C. Yan, Y. Ding, Y. Liu, G. Chen, G. Yu, Defect engineering metal-free polymeric carbon nitride electrocatalyst for effective nitrogen fixation under ambient conditions. *Angew. Chem. Int. Ed. Engl.* **57**, 10246–10250 (2018).
24. R. Geick, C. H. Perry, G. Rupprecht, Normal modes in hexagonal boron nitride. *Phys. Rev.* **146**, 543–547 (1966).
25. E. L. Spitler, W. R. Dichtel, Lewis acid-catalysed formation of two-dimensional phthalocyanine covalent organic frameworks. *Nat. Chem.* **2**, 672–677 (2010).
26. T. Sainsbury, A. Satti, P. May, Z. Wang, I. McGovern, Y. K. Gun'ko, J. Coleman, Oxygen radical functionalization of boron nitride nanosheets. *J. Am. Chem. Soc.* **134**, 18758–18771 (2012).
27. I. Sobczak, M. Kozlowska, M. ZiolekAdam, Au containing mesostructured cellular foams NbMCF and ZrMCF inselective oxidation of methanol to formaldehyde. *J. Mol. Catal. A Chem.* **390**, 114–124 (2014).
28. G. S. Foo, G. Hu, Z. D. Hood, M. Li, D. Jiang, Z. Wu, Kinetics and mechanism of methanol conversion over anatase titania nanoshapes. *ACS Catal.* **7**, 5345–5356 (2017).
29. G. V. Isaguliants, I. P. Belomestnykh, Selective oxidation of methanol to formaldehyde over V–Mg–O catalysts. *Catal. Today* **100**, 441–445 (2005).
30. T.-J. Yang, J. H. Lunsford, Partial oxidation of methanol to formaldehyde over molybdenum oxide on silica. *J. Catal.* **103**, 55–64 (1987).
31. Y. Fu, J. Shen, Selective oxidation of methanol to dimethoxymethane under mild conditions over V_2O_5/TiO_2 with enhanced surface acidity. *Chem. Commun.* , 2172–2174 (2007).
32. J. Florek-Milewska, P. Decyk, M. Ziolek, Catalytic properties of Cu/SBA-3 in oxidative dehydrogenation of methanol—The effect of the support composition. *Appl. Catal. A Gen.* **393**, 215–224 (2011).
33. C. Brookes, P. P. Wells, G. Cibin, N. Dimitratos, W. Jones, D. J. Morgan, M. Bowker, Molybdenum oxide on Fe_2O_3 core–shell catalysts: Probing the nature of the structural motifs responsible for methanol oxidation catalysis. *ACS Catal.* **4**, 243–250 (2014).
34. Y. Cao, W.-L. Dai, J.-F. Deng, The oxidative dehydrogenation of methanol over a novel Ag/SiO_2 catalyst. *Appl. Catal. A Gen.* **158**, L27–L34 (1997).
35. W. Qi, W. Liu, X. Guo, R. Schlogl, D. Su, Oxidative dehydrogenation on nanocarbon: Intrinsic catalytic activity and structure–function relationships. *Angew. Chem. Int. Ed.* **54**, 13682–13685 (2015).
36. W. Qi, W. Liu, B. Zhang, X. Gu, X. Guo, D. Su, Oxidative dehydrogenation on nanocarbon: Identification and quantification of active sites by chemical titration. *Angew. Chem. Int. Ed.* **52**, 14224–14228 (2013).
37. L. Shi, D. Wang, A.-H. Lu, A viewpoint on catalytic origin of boron nitride in oxidative dehydrogenation of light alkanes. *Chin. J. Catal.* **39**, 908–913 (2018).
38. R. Huang, B. Zhang, J. Wang, K.-H. Wu, W. Shi, Y. Zhang, Y. Liu, A. Zheng, R. Schlögl, D. S. Su, Direct insight into ethane oxidative dehydrogenation over boron nitrides. *ChemCatChem* **9**, 3293–3297 (2017).
39. O. Baake, P. S. Hoffmann, A. Klein, B. Pollakowski, B. Beckhoff, W. Ensinger, M. Kosinova, N. Fainer, V. S. Sulyaeva, V. Trunova, Chemical character of BC_xNy layers grown by CVD with trimethylamine borane. *X-Ray Spectrom.* **38**, 68–73 (2009).
40. Y. Gao, G. Hu, J. Zhong, Z. Shi, Y. Zhu, D. S. Su, J. Wang, X. Bao, D. Ma, Nitrogen-doped sp^2-hybridized carbon as a superior catalyst for selective oxidation. *Angew. Chem. Int. Ed.* **52**, 2109–2113 (2013).
41. R. Franke, S. Bender, J. Hormes, A. A. Pavlychev, N. G. Fominych, A quasi-atomic treatment of chemical and structural effects on K-shell excitations in hexagonal and cubic BN crystals. *Chem. Phys.* **216**, 243–257 (1997).
42. R. Franke, S. Bender, H. Jüngermann, M. Kroschel, M. Jansen, The determination of structural units in amorphous Si–B–N–C ceramics by means of Si, B, N and C K–XANES spectroscopy. *J. Electron. Spectrosc. Relat. Phenom.* **101-103**, 641–645 (1999).
43. G. Kresse, J. Hafner, *Ab initio* molecular dynamics for liquid metals. *Phys. Rev. B* **47**, 558 (1993).

44. G. Kresse, D. Joubert, From ultrasoft pseudopotentials to the projector augmented-wave method. *Phys. Rev. B* **59**, 1758 (1999).
45. J. P. Perdew, K. Burke, M. Ernzerhof, Generalized gradient approximation made simple. *Phys. Rev. Lett.* **77**, 3865–3868 (1996).
46. J. K. Nørskov, J. Rossmeisl, A. Logadottir, L. Lindqvist, J. R. Kitchin, T. Bligaard, H. Jónsson, Origin of the overpotential for oxygen reduction at a fuel-cell cathode. *J. Phys. Chem. B* **108**, 17886–17892 (2004).
47. Á. Valdes, Z.-W. Qu, G.-J. Kroes, J. Rossmeisl, J. K. Nørskov, Oxidation and photo-oxidation of water on TiO_2 surface. *J. Phys. Chem. C* **112**, 9872 (2008).

Acknowledgments
Funding: The authors acknowledge financial support from the National Natural Science Foundation of China (21761132010, 91645114, 21573256, 21571035, 21673040, and 51521091) and the Youth Innovation Promotion Association, Chinese Academy of Sciences. B.J.M.E. and F.H. acknowledge the funding of part of the research by the Deutsche Forschungsgemeinschaft (DFG; German Research Foundation) within project ET-101/13-1.

Author contributions: X.Z., W.Q., and Z.X. designed the experiments. W.Q. and Z.X. supervised the project. X.Z., P.Y., F.L., and W.Q. performed the experiments. J.X. and S.L. performed DFT calculations. All authors discussed the experiments and results. X.Z., P.Y., W.Q., and Z.X. prepared and revised the manuscript. **Competing interests:** The authors declare that they have no competing interests. **Data and materials availability:** All data needed to evaluate the conclusions in the paper are present in the paper and/or the Supplementary Materials. Additional data related to this paper may be requested from the authors.

Submitted 15 December 2019
Accepted 12 May 2020
Published 24 June 2020
10.1126/sciadv.aba5778

Citation: X. Zhang, P. Yan, J. Xu, F. Li, F. Herold, B. J. M. Etzold, P. Wang, D. S. Su, S. Lin, W. Qi, Z. Xie, Methanol conversion on borocarbonitride catalysts: Identification and quantification of active sites. *Sci. Adv.* **6**, eaba5778 (2020).

Methanol conversion on borocarbonitride catalysts: Identification and quantification of active sites

Xuefei Zhang, Pengqiang Yan, Junkang Xu, Fan Li, Felix Herold, Bastian J. M. Etzold, Peng Wang, Dang Sheng Su, Sen Lin, Wei Qi and Zailai Xie

Sci Adv **6** (26), eaba5778.
DOI: 10.1126/sciadv.aba5778